

VALIDATION OF A TRANSONIC ANALYSIS CODE FOR USE IN  
PRELIMINARY DESIGN OF ADVANCED TRANSPORT CONFIGURATIONS

Edgar G. Waggoner  
Leader, Applied Aerodynamics Group  
NASA Langley Research Center  
Hampton, Virginia

ABSTRACT

The WBPPW code has the capability of analyzing flow-field effects about configurations which include wing pylons and engine nacelles or pods in addition to the basic wing/fuselage combination. Using the concept of grid embedding, the code solves the extended small disturbance transonic flow equation for complex flow interactions of the various configuration components. A general description of the code and solution algorithm is included. Results are presented and compared with experiment for various configurations which encompass the code capabilities. These include wing planform and wing contour modifications and variations in nacelle position beneath a high-aspect-ratio wing. Results are analyzed in the light of preliminary design, where the capability to accurately compute flow-field effects resulting from various configuration perturbations is important. The comparisons show that the computational results are sensitive to subtle design modifications and that the code could be used as an effective guide during the design process for transport configurations.

NOMENCLATURE

Symbol

AR	aspect ratio
b	wing span
c	local wing chord
$C_D$	total configuration drag coefficient
$C_L$	total configuration lift coefficient
$C_M$	total configuration pitching moment coefficient
$C_p$	pressure coefficient
M	Mach number
MFR	nacelle inlet mass flow ratio
NPR	nacelle nozzle pressure ratio
R	radius
u,v,w	perturbation velocities
U,V,W	transformed velocity components
X,Y,Z	physical coordinates
$\alpha$	angle of attack
$\gamma$	specific heat ratio
$\Delta$	increment
$\delta^*$	boundary layer displacement thickness
n	normalized spanwise coordinate
$\phi$	perturbation velocity potential

Subscripts

b	actual body
c	computational body
e	exhaust
i,j,k	mesh indices
J	jet
x,y,z,r	partial derivative
$\infty$	freestream

INTRODUCTION

The role which computational fluid mechanics plays within the aerodynamic design process has been expanding rapidly over the past decade. This expansion has been the product of growth in the capabilities of computer codes and acceptance of their use in the design process by the design community. Innovations in structuring solution algorithms, increases in computational efficiencies, and growth in computer memory capacity have interacted to yield computer codes which are used to solve complex fluid flow problems routinely. In addition, the design community has realized the complementary nature of experimental testing and numerical simulation.

This complementary nature is fairly apparent when one addresses the expenses and risks associated with configuration development. One of the major advantages of numerical solutions compared to experimental testing is the relative ease of modifying a configuration. This capability allows a designer to investigate many configurations or perturbations to a given configuration in a relatively short time. With this added flexibility, a design problem may be thought of from a different perspective. Preliminary analysis may encompass a much larger design space, thereby increasing the possibility of a target design being included in the design space. The space may then be reduced computationally to a size that is commensurate with the accuracy and validity of the computational tool. Experimental refinement and verification are then performed in a much smaller design space, reducing both the cost and the time required.

However, before a code can be accepted and used by the design community, the sense in which the results of the code can and should be interpreted and used must be addressed. It is important for the aerodynamicist to understand the effects that numerical and phenomenological errors inherent in a code have on resulting solutions. Through this type of understanding one can define the boundaries of applicability of a computer code with more precision. The present study involves validation of a small-disturbance transonic analysis code, WBPPW, developed by Charles Boppe of Grumman Aerospace, which has the capability of computing flow fields around wing/body configurations with installed pods or engine nacelles and pylons<sup>1</sup>. Specifically, the effects of wing-planform and root-section modifications and the addition of a nacelle/pylon on an advanced transport configuration have been computed and compared with experimental results. Code capabilities are viewed in the light of preliminary design where extensive reliance on computations is not uncommon. This, of course, leads to a detailed

design phase where the balance of the emphasis is on experimental verification and refinement.

Subsequent sections include a general description of the WBPPW code. Comparisons of computational and experimental wing pressure distributions are presented showing the effects of modifying the wing section and planform, of adding an engine nacelle/pylon combination, and of varying the nacelle position longitudinally and vertically. Comments are also included relative to efforts to determine detailed nacelle surface pressure distributions. The experimental data used in this study were obtained from tests in the NASA Langley Research Center 8-Foot Transonic Pressure Tunnel.

### CODE DESCRIPTION

#### Governing Potential Flow Equation

Using finite difference approximations, a modified transonic small disturbance flow equation is iteratively solved in the embedded grid systems. Extra terms, which are found in the full potential equation, are retained to improve resolution of swept shock waves and to predict the equation type (elliptic or hyperbolic) more accurately. The governing potential flow equation is:

$$\begin{aligned} & [1 - M_\infty^2 - (\gamma + 1)M_\infty^2 \phi_x - \frac{\gamma + 1}{2} M_\infty^2 \phi_x^2] \phi_{xx} \\ & - 2M_\infty^2 \phi_y \phi_{xy} + [1 - (\gamma - 1)M_\infty^2 \phi_x] \phi_{yy} + \phi_{zz} = 0 \end{aligned} \quad (1)$$

### COMPUTATIONAL GRID SYSTEMS

#### Crude Grid System

The computational space used in the method is filled with a relatively crude global grid system. This grid is stretched to planes corresponding to infinity in all directions. The global grid basically serves two purposes. It provides the proper representation of the effects of the configuration on the far field and conversely, the effects of the far-field boundary conditions on the flow field near the configuration. In addition, the crude grid provides the channels of communication between the various embedded fine grids. A Dirichlet boundary condition,

$$\phi = 0 \quad (2)$$

is imposed on all boundary planes except the downstream plane and the plane of symmetry. On the downstream plane, the boundary condition is of the form

$$\phi_{yy} + \phi_{zz} = 0. \quad (3)$$

At the plane of symmetry, the flow must not have a velocity component which would allow the flow to cross the plane of symmetry. Hence, the following

equations are enforced:

$$\phi_y = 0 \quad (4)$$

$$\phi_{xy} = 0 \quad (5)$$

A successive line overrelaxation (SLOR) scheme is used to solve the governing equation. The solution is obtained successively on vertical lines from fore to aft at a given spanwise location. When the solution is being obtained on the crude grid system, span stations are solved successively starting outboard and moving toward the symmetry plane. This direction is reversed when the solution is being obtained on the fine wing grid system.

#### Wing Fine Grid System

Fine grid systems around components of interest are embedded in the global, continuous grid, figure 1. The grids are distributed along the wing span and, if desired, may also encompass the fuselage, pylon, or pod. Within the fine grids, the resolution is much enhanced relative to the global grids. This allows far greater resolution in areas where flow-field gradients are large.

Each of the fine grids is independent and sized according to the geometry of the component it encompasses. The extent of the fine wing grid is based on the local chord. Boundaries are established 20 percent of the local chord in front of each wing section and 10 percent behind the trailing edge. The upper and lower limits of the individual fine wing grids are set at 30 percent and 10 percent of the wing average chord, respectively. Resolution in the streamwise direction is such that 100 grid points fall between the leading and trailing edges of the local wing section. Under most circumstances, there will be 25 grid points in the vertical direction. The leading and trailing edges of the wing fall midway between streamwise mesh points. The wing fine grids are set up at spanwise locations which correspond to crude grid spanwise planes. For a wing alone analysis, 18 fine grid arrays would fall on the wing. For analysis of a wing/fuselage configuration, the number of fine grid arrays falling on the wing would depend on the relative size of the wing span and fuselage radius. A typical fine wing grid is shown in figure 2a.

#### Body Fine Grid System

The fine body grid, figure 2b, surrounds the entire fuselage or portions of the fuselage at the user's option. For normal applications, the fine body grid extends from 10 percent of the body length forward of the nose to 10 percent behind the tail. The user does have the option, however, to concentrate the grid around some particular fuselage region. Top, bottom, and side fine body grid boundaries are established approximately one average body radius away from the body surface. The individual fine body grid arrays are similar to the wing fine grid arrays, being evenly spaced in each direction. Again, it should be pointed

out that it is through the interaction of the global grid and fine grid systems that the influence of various components are integrated into the solution.

### Nacelle and Pylon Fine Grid System

Flow field resolution around a pod or engine nacelle is available in two modes. If the effect of the pod on the wing or fuselage is the objective of a given analysis, then a crude grid representation of the pod would be sufficient. However, if detailed pressure distributions on the pod surface are the objective, then a fine grid solution should be obtained. Figure 3 presents the crude and fine grid arrangement for pods and nacelles. The representation of the pod surface in the crude grid is made up of the eight grid points closest to the pod surface. The number of axial pod stations is a function of the pod length relative to other configuration components which are used to generate the global grid. For typical engine nacelles found on transport aircraft, 10 to 20 mesh points will fall along the nacelle in the axial direction.

The fine pod grid is similar to the fine body grid. Each grid plane in the Y-Z plane is 17x17. This density and arrangement of grid points allows the pod cross-section surface to be represented by approximately 28 grid points at each axial plane, contrasted to 8 grid points in the crude grid. There are 132 axial planes which make up the fine pod grid. Of these, 100 planes actually fall on the pod. Global crude grid potentials are interpolated to determine the fine pod grid perimeter potentials. The fine pod grid is relaxed and the flow field potentials updated. These updated potentials from the fine pod grid are used to update the crude grid potentials making up the inner boundary of the overlap region between the two grid systems. The crude grid now has updated potentials on the inner boundary which are held fixed as the crude grid is relaxed. This process continues to cycle until both grid systems are converged.

Additional boundary conditions must be supplied for the inlet and exhaust faces for engine nacelles. Two options are available for simulating exhaust effects. The exhaust may be assumed to be cold, as typically found in wind-tunnel testing, or hot, as found in flight-test results. Expressions are derived in reference 1 for the exhaust jets and presented below:

$$V_{J\text{COLD}} = \sqrt{\frac{1 - (1/\text{NPR})^{0.2857}}{1 - (1/(1 - 0.2 M_\infty^2))}} \quad (6)$$

$$V_{J\text{HOT}} = 2.0636 \sqrt{\frac{1 - (1/\text{NPR})^{0.2481}}{1 - (1/(1 - 0.2 M_\infty^2))}} \quad (7)$$

With a three point extrapolated difference scheme, an expression for the flow field potential at the exhaust face is determined to be

$$\phi_{I_e} = \frac{2(1 - V_J)\Delta X + 4\phi_{I_e+1} - \phi_{I_e+2}}{3} \quad (8)$$

where grid point  $I_e$  is on the exhaust face and  $I_e + 1$  and  $I_e + 2$  are just downstream.  $V_J$  is determined from equation 6 or 7 above.

The inlet mass flow ratio provides a relationship to determine the inlet velocity as

$$\frac{V_I}{V_\infty} = \text{MFR} \quad (9)$$

With this relationship and a three point extrapolated difference scheme, the expression

$$\phi_{I_i} = \frac{2(\text{MFR} - 1)\Delta X + 4\phi_{I_i-1} - \phi_{I_i-2}}{3} \quad (10)$$

can be derived for the flow field potential at the inlet face, where  $I_i$  designates the grid point at the inlet face and  $I_i - 1$  and  $I_i - 2$  are grid points just upstream of the inlet face. For closed bodies, the inlet and exhaust velocities are set to zero, and equations 8 and 10 are again used to compute the flow potentials around the nose and tail.

Computations have shown that, in order to accurately compute the interference effects between a nacelle and wing, the distance between the wing and nacelle must be carefully modeled. For this reason, the vertical grid is adjusted to insure that the nacelle height (distance between wing and nacelle) is accurately modeled in the computations. The vertical grid is interrogated to determine the closest grid point beyond the nacelle centerline relative to the wing plane. The vertical grid is then compressed to make this grid point coincident with the centerline of the nacelle. In the spanwise direction, the positioning of the nacelle or pod is not as critical as vertical positioning except in cases where pod/pod or fuselage/pod interference is important. The spanwise grid system used for wing/body applications is not altered when a nacelle or pod is added to the configuration. The 18 spanwise mesh planes which fall on the wing remain fixed, with the wing tip centered between two mesh planes. This results in a required shift of the nacelle from its actual position to the closest mesh plane, which can be as much as 3.5 percent of the semispan. In general, differences of this magnitude in spanwise location will not cause any problem. However, as stated above, for certain types of configuration analysis, the shift may significantly change the spanwise displacement of interfering surfaces.

### Wing Viscous Effects

The WBPPW analysis code has the capability of including the effects of viscosity into the solution. Basically, the boundary layer effects are included into the solution process by modifying the wing surface boundary conditions.

The slope of the displacement thickness,  $\frac{\partial \delta^*}{\partial X}$ , is

added to the boundary condition on the wing surface. This modifies the wing surface to an equivalent "fluid" wing shape which is then analyzed by the potential flow part of the code. A modified Bradshaw boundary layer computation is used to provide details of the viscous layer on the wing surface. The calculations are based on the method developed by Mason<sup>2</sup>. Two-dimensional boundary layer computations are modified to include sweep effects by use of an infinite sheared wing approach to extend the computations. The sweep angle used for the calculations is the local sweep of the wing mid-chord line.

The laminar boundary layer is calculated by the Thwaites method modified for compressible flow. Turbulent boundary layers are computed by the two-dimensional Bradshaw turbulent boundary layer method. The modified chord technique of Nash and Tseng<sup>3</sup> is applied to each method to determine the flow about an infinite yawed wing.

Boundary layer computations terminate when separation is detected in the turbulent boundary layer (shear stress vanished). For conventional wing sections, the slope of the displacement thickness is simply extrapolated to the trailing edge. However, many wings of current interest employ supercritical sections. For boundary layer separation in the cusp region of supercritical wings, the above extrapolation scheme is not accurate. In this case, Bavitz's empirical relation<sup>4</sup> is used to approximate the displacement thickness distribution in the cusp region. Bavitz's relation is based on an extensive correlation study of supercritical airfoils.

It should be noted that the use of the empirical or extrapolation techniques for separated flow is only to allow the solution process to continue. Often these corrections may be such that subsequent boundary layer calculations may not show any separation.

### Solution Process

To obtain a solution for any configuration, the configuration is initially analyzed in the crude grid system. The general characteristics of the flow field can be established fairly quickly in this manner while minimizing computer resources. This yields the starting solution for the crude grid/fine grid interaction. For the initial fine grid relaxation, the fine grids are filled by linear interpolation from the crude grid system. After the initial solution, only the boundary potential values are updated from the crude grid system. The solution process is described below for a complete wing/body/nacelle/ pylon configuration.

1. The configuration is first analyzed in the crude grid system. Potentials from this analysis are used to fill the wing and nacelle fine grids.
2. The fine wing grid system is relaxed employing Dirichlet boundary conditions (potentials obtained from the crude grid) at the outer boundaries. Neumann boundary conditions are enforced at the wing plane.

3. Viscous calculations are performed on the wing, if desired.
4. The nacelle fine grid system is relaxed. Outer boundary potentials are determined from the crude grid solution. Flow field potentials, corresponding to inlet and exit velocities, are computed for the inlet and exhaust faces and also used as boundary conditions.
5. The crude grid is updated to reflect the results of steps 2 through 4. Updated boundary potentials from the fine wing and nacelle grid solutions are used as Dirichlet boundary conditions during the crude relaxation cycle. The crude grid relaxation provides potentials to be used as perimeter values for the fine grids.

Steps 2 through 5 are repeated until the flow field solution is converged.

### Pressure Coefficient Calculations

Pressure coefficients on the wing and pylon are computed using the following relationships:

$$C_{p_{wing}} = -2\phi_x + (1 - M_\infty^2)\phi_x^2 + \phi_y^2 \quad (11)$$

$$C_{p_{pylon}} = -2\phi_x + (1 - M_\infty^2)\phi_x^2 + \phi_z^2 \quad (12)$$

The velocity components on the body or nacelle are computed similarly; however, additional corrections are applied to account for the fact that the computations do not take place on the true body surface. The corrections relate the differences in the actual body radius and the computational body radius to account for local velocity differences on the computational body and actual body. Velocity distributions on the computational body are calculated using central difference operations. The velocity on the actual body is computed using the following relationship:

$$u_b = \phi_{x_b} = \phi_{x_c} + (R_b - R_c) \left( \frac{R_b}{R_c} \phi_r \right)_b \quad (13)$$

The pressure coefficient on the body is then calculated with the equation

$$C_p = -2\phi_{x_b} + (1 - M_\infty^2)\phi_{x_b}^2 \quad (14)$$

It is important to note that the empirical corrections in equation 13 can become quite large when the actual and computational body surfaces deviate significantly. This is apparent in the nose region of a closed body. A complete description of the development of the above equations is included in reference 5.

### Computer Resources

The WBPPW code is operational on both the CDC CYBER 175 and 203 systems at NASA Langley Research Center. On the CYBER 175, the code is segmented and requires approximately 100,000 words of memory

for loading and execution. It is important to consider the code segmentation for a small machine. This has to be done very carefully to avoid excessive peripheral process overhead charges during execution. The CYBER 203 is a vector, virtual-memory machine. On this machine, the code requires 550,000 words of memory for loading and execution. No attempt has been made to take advantage of the vector processing capabilities of this machine. The primary reason for this is the relatively short vector lengths available without significant restructuring of the solution algorithm. Table I presents typical run times per iteration for various configurations on the two CYBER machines. In order to approximate the total run time for a solution, the run time per iteration should be multiplied by the sum of the crude grid iterations plus twice the number of crude/fine iterations.

## COMPUTATIONAL RESULTS

### Wing/Body Results

#### Design Problem and Computational

Description. From the family of supercritical wings tested at NASA Langley Research Center in support of the EET program, one was chosen for further experimental development. This selected configuration, also the baseline wing for this study, has a wing 14.4-percent thick at the root and 10.6-percent thick at the tip. Designed for a cruise lift coefficient of 0.57 at  $M = 0.80$ , the wing had an aspect ratio of 9.8 and quarter chord sweep of  $30^\circ$ . The wing planform and root section contour are shown in figure 4.

In an effort to maximize the depth of the wing root, both a leading and trailing edge extension were added to the selected configuration. Thick root sections not only minimize structural weight but facilitate the problem of landing gear storage. For the trailing edge extension, the trailing edge of the wing was completely unswept from the wing root outboard to the 40-percent span station. Thickness was then added, primarily to the lower surface, so that the thickness to chord ratio at the root was not changed. Modifications to the planform and root airfoil are shown in figure 4. The airfoil contour change was faired into the baseline wing contour gradually, such that outboard of 40-percent semispan the two wings were the same. Since the baseline wing exhibited aerodynamic characteristics which were desired at that time, this change was to be accomplished with as small a change to the wing aerodynamic characteristics as possible.

In adding the leading-edge extension, the wing root was again thickened such that  $t/c$  did not vary significantly. The increase in sweep, however, did provide an increase in drag rise Mach number. The chord at the wing root was increased 12 percent and the leading-edge sweep increased from  $31^\circ$  to  $37^\circ$  inboard of 43-percent semispan. Again, these changes were gradually faired into the baseline wing contours. Refer once more to figure 4 for these modifications.

Considerable experimental data existed on these configurations<sup>6</sup>. The problem addressed

computationally was to analyze each of the designs at comparable conditions. The results could then be compared with existing experimental data. The objective, as previously stated, was to evaluate the sensitivity of the analysis code to the planform and wing contour changes described above. Since force and pressure data were available, comparisons between total configuration forces and moments and wing pressure distributions could be made. Thus, not only the absolute levels of the predictions could be compared, but equally important for this study, the incremental changes between the three configurations could be evaluated. Through these comparisons, the suitability of using the code as a design aid could be evaluated.

Computational Procedures. In order to obtain computational results which were consistent for the various configurations, a set of guidelines was established to ensure that computationally the configurations were treated identically. After reviewing the available experimental data, it was apparent that pressure data had been obtained at the same angles of attack for each configuration. This turned out to be advantageous for the study being undertaken. Each configuration was to be analyzed at the same geometric angle of attack as the experiment. This would afford the opportunity to observe how well the code predicted the actual levels of forces and pressures, and also the incremental changes between configurations, while keeping angle of attack constant.

An angle of attack and Mach number were chosen for the analysis conditions which were very near the design point for the baseline wing,  $\alpha = 2.2^\circ$  and  $M = 0.82$ . The analysis code was run at the experimental angle of attack at a slightly elevated freestream Mach number. The Mach number shift was an attempt to account for the fuselage effect, which was not modeled in the code when only a crude body grid was used. The value of the Mach number shift ( $\Delta M = .007$ ) was determined by analyzing an axisymmetric body having the same area distribution as the fuselage used in the experiment with a transonic potential flow code for bodies<sup>7</sup>. A weighted average of the Mach shift over the wing plane was used to calculate the freestream shift applied to the analysis conditions.

Viscous effects were modeled in the computations by coupling the potential flow and the boundary layer calculations. The experimental Reynolds number  $2.4 \times 10^6$  based on the wing mean aerodynamic chord was matched in the analysis. Attempts were also made to model the experimental transition locations on the upper and lower surface but were not always successful. Natural transition was predicted on the upper surface at several span stations for each configuration. This was not observed during the experiment. However, the effect on the calculated pressures is not thought to be significant. On the lower surface, the code consistently predicted separation in the cove region. When this occurred for a supercritical section, an empirical relation developed by Bavitz<sup>4</sup> was used to approximate the displacement thickness in the cove region. This allowed the solution to continue using a displacement thickness which had approximately the correct

shape. Once again, the separation was not apparent in the experiment. However, the strong spanwise flow in the cusp region of the wings was observed. This had a relieving effect on the boundary layer. The boundary layer code used a 2-D analysis theory. Hence, the relief from crossflow was not modeled. The boundary layer ended up being significantly thicker in this region, contributing to the prediction of separation by the code.

Each solution was run in exactly the same manner to insure that no bias occurred between the solutions due to the procedure. The solution for each configuration was relaxed 150 times on the crude grid. Then 250 crude/fine iterations were performed in the inviscid mode. For the next 120 iterations, a boundary layer displacement thickness was calculated every 20 iterations. The displacement thickness slopes were underrelaxed by a factor of 0.6 and included in the solution as a modification to the boundary condition on the wing surface. Finally, the solution was relaxed an additional 100 iterations without updating the displacement thickness slopes. Following this procedure allowed solutions to be attained where the average update to the flow field potential was less than  $.3 \times 10^{-6}$ .

Comparisons of Computations with Experimental Data. As discussed in the previous section, the comparisons of the computations were to be made in two manners. The levels of the predictions were compared with experimental data, and the incremental changes between the configurations were also compared. Pressure distributions were compared at two spanwise locations. One was about midway between the body and the wing break, and the second was at the edge of the wing modifications where the modified section faired into the baseline wing.

The pressure distributions for the baseline wing and the trailing edge modifications are presented in figures 5 and 6. The differences in the pressure distributions are very subtle. At the inboard span station, the experiment shows the shock moving slightly aft on the modified configuration and a little less expansion in the mid-chord region of the lower surface. The computations predict opposite trends at the inboard station. The shock moves forward slightly and the lower surface shows expanded pressures along the lower surface for the modified configuration. However, the overall difference in pressure distributions between the two configurations is small. At the outboard span station, the differences shown in the experiment are almost nonexistent. Again, noticeably expanded pressures are evident in the computations for the lower surface of the modified configuration. As before, however, the differences in the pressure distributions are very slight.

The modification to the wing leading edge yields significant changes in the wing pressure distribution, as shown in figures 7 and 8. The inboard distribution, depicted in figure 7, shows a reduced leading-edge expansion and significant reduction of shock strength on the upper surface. Associated with the reduction in shock strength is a forward movement of the compression of approxi-

mately 20-percent chord and an increase in the pressures (less negative) in the plateau region. The pressures on the lower surface are somewhat compressed along the chord for the leading-edge extension relative to the trailing-edge extension. Each of these characteristics is predicted by the analysis code.

The characteristics change slightly for the outboard distribution depicted in figure 8. The flow about the leading edge is expanded for the leading-edge modifications. This is evident in the experiment and in the calculations. The shock in the experiment almost disappears for the leading-edge extension, while the theory predicts a shock of approximately the same strength but moved forward relative to the trailing-edge modification. The flow is again slightly compressed on the lower surface. The trends are predicted quite well by the theory, and the levels and magnitudes of the pressure coefficients are accurate.

The incremental changes in the experimental forces and moments and computational predictions for the three configurations are presented in Table II. The same reference area and length are used to reduce the forces and moments for each configuration. In addition, the moment reference point is in the same location. This allows direct comparison of incremental coefficients between each configuration.

The code predicted a lift coefficient loss of .038 between the baseline wing and trailing-edge modification. Experimentally, the loss was approximately half of that amount. However, the loss from the baseline configuration to the leading-edge modification (denoted by the total length of the bar) was predicted within 10 percent. The loss in lift for the trailing-edge extension is apparent from an observation of the lower surface pressure distributions, shown in figures 5 and 6, which exhibited over-expanded pressures relative to the experiment.

The incremental moments show the differences in pitching moment at a constant angle of attack. The differences for each of the modifications are predicted within .01 moment coefficient of the experimental data. The influence that the lower surface cusp pressures have on the pitching moment is obvious. This is an area where the 2-D boundary layer approximations could well be improved.

The incremental drag data presented in Table II shows excellent agreement. Each of the increments is predicted within 5 counts. Although caution should be exercised when attempting to use the absolute levels of the drag predictions, the increments in this case were predicted quite well.

Reference 8 presents a complete description of this validation effort and more extensive data comparisons.

#### Wing/Body/Pylon/Nacelle Results

Validation of the pylon/nacelle option in the code was accomplished by comparing results obtained using the analysis code with data

obtained during the experimental research performed by Patterson and Flechner<sup>9</sup> in support of the Energy Efficient Transport effort at NASA Langley Research Center. The baseline configuration is an advanced transport configuration developed at Langley, as shown in figure 9. The wing is swept 30° at the quarter-chord, has an aspect ratio of 10, and is 12-percent thick at the nacelle location of 40-percent semispan. Two different nacelles were analyzed and compared with experimental data. The E<sup>3</sup> mixed-flow engine nacelle, depicted in figure 10a, was analyzed at three positions; and the LCSF engine nacelle, shown in figure 10b, was analyzed at two positions below the wing (see figure 11). Each of the nacelles was mounted on a pylon with an NACA 4412 cross section.

The wing/body configuration without nacelles or pylons was first analyzed to ensure that the basic flow field characteristics were predicted by the analysis code. Flow conditions identical to those to be used in the nacelle analysis were simulated in the code; that is, no attempt was made to match the lift on the wing for the comparisons. Results are presented in figure 12 at  $M = 0.82$  and an angle of attack of 2.8° at both an inboard and outboard span station. The analysis agreed quite well with the experimental data.

The wing/body/pylon/nacelle combination was analyzed and comparisons made to show the effect of adding a nacelle to a wing/body configuration. Located spanwise at 40 percent of the semispan, the E<sup>3</sup> nacelle was positioned such that the nacelle centerline was 0.4 chord below the wing plane. The exit plane of the nacelle was longitudinally located at 0.17 chord. Analytical and experimental pressure distributions for locations just inboard and outboard of the pylon are presented in figures 13a and 13b, respectively. Since a pylon was modeled for the configuration, the nacelle is only modeled in the crude grid system. On the upper surface, the most noticeable observation is the increase in the pressures (less negative) from the leading edge back to the shock. The compression observed experimentally in the wing/body/nacelle analysis is not accurately predicted with the computations; however, the trend of the compression, followed by a flow expansion, is predicted computationally. The upper surface experimental data are the same on either side of the pylon.

Expanded pressures are observed at the leading edge on the lower surface when the nacelle is added to the configuration. Computations predicted a greater expansion inboard than outboard while the experiment showed the opposite trend. Over the mid-chord region on the lower surface, the analysis and experiment showed increased (less negative) pressures after the nacelle was added. In the wing cove region, the pressures are slightly elevated back to the trailing edge with the nacelle configuration. Again, the same trends are observed in the computations and experimental data.

The next set of comparisons, which are presented in figure 14, show the results of moving the E<sup>3</sup> nacelle aft 10 percent of the local chord while maintaining the same vertical spacing rela-

tive to the wing. Upper surface pressures show little effect from the nacelle movement. Experimentally, the pressures are more negative near the leading edge for the aft location. The computations show only a very slight decrease in the leading-edge pressures.

Effects of moving the nacelle aft are more pronounced on the lower surface pressures. The leading-edge pressures are decreased and cusp pressures are slightly increased due to the aft position. These effects are predicted by the analysis code; however, the magnitude of the leading-edge effect is underpredicted. Peaks observed in the lower surface leading-edge pressure distribution are strongly influenced by the pod/pylon/wing interaction. Hence, it is not surprising that the magnitude of this effect is not accurately predicted, although the trend does show up in the computations.

Data showing the effects of shifting the LCSF nacelle forward 15 percent and down 5 percent of the local chord relative to the original position described above are presented in figure 15. Along the wing upper surface, the data do not indicate significant effects resulting from the nacelle movement. At the leading edge, the lower surface pressures indicate less flow expansion than for the original nacelle position. The magnitude of the reduced expansion is not as great in the experimental data as predicted by the WBPPW code. Following the flow expansion, the computations show a compression back to approximately 30-percent chord that is not observed in the experimental data. Overall, the computational data show a greater effect from the nacelle movement than is evident in the experimental data. Again, however, the trends are predicted sufficiently on the lower surface. A more detailed account of this study, including more comparisons of computations and experimental data, is included in reference 10.

#### CAVEATS AND RECOMMENDATIONS

There are specific limitations inherent in the basic formulation of the code. These generally result from computer storage limitations which preclude extension of the solution algorithm to certain configurations. The most important of these will be delineated in the following paragraphs.

Calculations are available for only one fine body grid system. That is, though one may model a configuration with multiple nacelles and a fuselage, only one nacelle on the fuselage can be modeled in the fine body grid system. The user is limited to modeling configurations with no more than two pods or nacelles per side. The pylon is modeled as having a rectangular planform. This limitation is being addressed by the code developers, who are extending the code to handle swept- and tapered-pylon planforms. If a nacelle is modeled in the nacelle fine grid system, the pylon cannot be modeled. This and the pylon planform limitations are rather severe since both have significant impact on nacelle pressure distributions. Neither canards nor horizontal or vertical tail surfaces can be modeled. However, Airdala of Grumman has developed a wing/canard

extension to the code<sup>11</sup> and is currently working to extend the code to handle an empennage.

The problems associated with deriving meaningful results from a transonic analysis code are often not trivial. These complex codes do not lend themselves to a "black-box" approach to analysis. That is, one may input a configuration, turn a key, and obtain a solution; however, the resulting solution should be carefully scrutinized before accepting the results as valid. The ability to do this comes with experience in using the code. The wise user gains insight into the use of the code by first analyzing simple shapes. More complex configuration analyses should be approached cautiously and conservatively. This is not meant to scare potential code users away from the code, but it is an attempt to make the user aware that meaningful results will most likely be obtained when the basic characteristics of the computer code and subject transonic flow field are understood. There is simply no substitute for experience when the user must make judgments concerning the cause of an unforeseen problem.

### CONCLUSIONS

The WBPPW code is a powerful computational tool which has a tremendous amount of flexibility. Wing pressure distributions have been computed on a wing/body configuration with three different planform variations and a wing/body/pylon/nacelle configuration employing various nacelle positions. Comparisons of computed and experimental wing pressure distributions indicate the code to be capable of predicting effects resulting from wing planform, wing section contour, and nacelle position variations from an advanced transport configuration. These results indicate that the code should be useful in providing guidance in a design environment. The following conclusions are emphasized:

1. The differences in wing pressure distributions resulting from wing planform and section contour variations were predicted by the code. The wing upper surface characteristics were predicted accurately, including shock location and strength, while less consistent results were obtained on the lower surface.
2. The trends and incremental changes for lift, drag, and pitching moment coefficient were consistently predicted for the planform and wing section contour variations.
3. The differences in wing pressure distributions resulting from the addition of the nacelle/pylon combination to the wing/body configuration were predicted in the computations.
4. Variations in wing pressure distributions resulting from nacelle translations were predicted. Effects of shifting the nacelle aft, as well as down, from a common position were analyzed. Trends were adequately predicted on the upper and lower surface wing pressure distributions.
5. Results were encouraging as far as using the code in a design environment. During this study it was observed that, where strong

interactions between components are evident, code convergence may require that several-hundred crude/fine iterations be run.

Use of this, as well as other computational methods, can significantly impact a design effort. However, computational techniques as they presently exist are not panaceas. Users must be knowledgeable and experienced to effectively apply a code and obtain meaningful results. A working knowledge of computational techniques and fluid mechanics is desirable for active participation in this area. However, the benefits which can be derived from a complementary program of experimentation and computation can be significant. When one realizes the financial risks associated with a new configuration development program, the benefits become apparent. Aside from the cost and time advantages that may be derived from computational analysis, the confidence associated with a design derived from a thorough experimental and computational program can have benefits which are immeasurable.

In summary, these points should be clear. Think of the code as a guide and supplement to experimental testing and not as a substitute. There is absolutely no substitute for experience with the code when it comes to interpreting results. Start with simple configurations and work up in complexity of configurations and severity of flow conditions. Finally, keep an open mind when interpreting results. No one claims any large complicated code is error free, so through understanding the physics of the flow being modeled and the characteristics of the solution algorithm, one can make a rational judgment relative to code accuracy for any given problem.

### Acknowledgement

The author wishes to acknowledge the assistance of D. W. Bartlett and J. C. Patterson of NASA Langley Research Center in providing assistance in working with the experimental data, and the aid of Charles Boppe of Grumman Aerospace Corporation in sharing his intimate knowledge of the WBPPW code.

### REFERENCES

1. Boppe, C. W.: Transonic Flowfield Analysis for Aircraft with Nacelles, Pylons, and Winglets. Proposed NASA CR.
2. Mason, W. H., et al.: An Automated Procedure for Computing the Three-Dimensional Transonic Flow Over Wing-Body Combinations, Including Viscous Effects. Air Force Flight Dynamics Laboratory Report AFFDL-TR-77-122, Vol. 1, October 1977.
3. Nash, J. F.; and Tseng, R. R.: The Three-Dimensional Turbulent Boundary Layer on an Infinite Yawed Wing. The Aeronautical Quarterly, November 1971, pp. 346-362.
4. Bavitz, P. C.: An Analysis Method for Two-Dimensional Transonic Viscous Flow. NASA TN D-7718, January 1975.



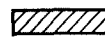

5. Boppe, C. W.: Transonic Flow Field Analysis for Wing-Fuselage Configurations. NASA CR 3243, May 1980.
6. Bartlett, D. W.: Wind-Tunnel Investigation of Several High Aspect-Ratio Supercritical Wing Configurations on a Wide-Body-Type Fuselage. NASA TM X-71996, 1977.
7. Keller, J. D.; and South, J. C.: RAXBOD: A Fortran Program for Inviscid Transonic Flow Over Axisymmetric Bodies. NASA TM X-72831, 1976.
8. Waggoner, E. G.: Computational Transonic Analysis for a Supercritical Transport Wing-Body Configuration. AIAA Paper No. 80-0129, January 1980.
9. Patterson, J. C.; and Flechner, S. G.: Advanced Aerodynamics and Active Controls, Selected NASA Research. NASA CP 2172, October 1980.
10. Waggoner, E. G.: Computational Transonic Analysis for an Advanced Transport Configuration with Engine Nacelles. AIAA Paper No. 83-1851, July 1983.
11. Aidala, P.: Numerical Aircraft Design Using 3-D Transonic Analysis with Optimization. AFWAL-TR-81-3091, August 1981.

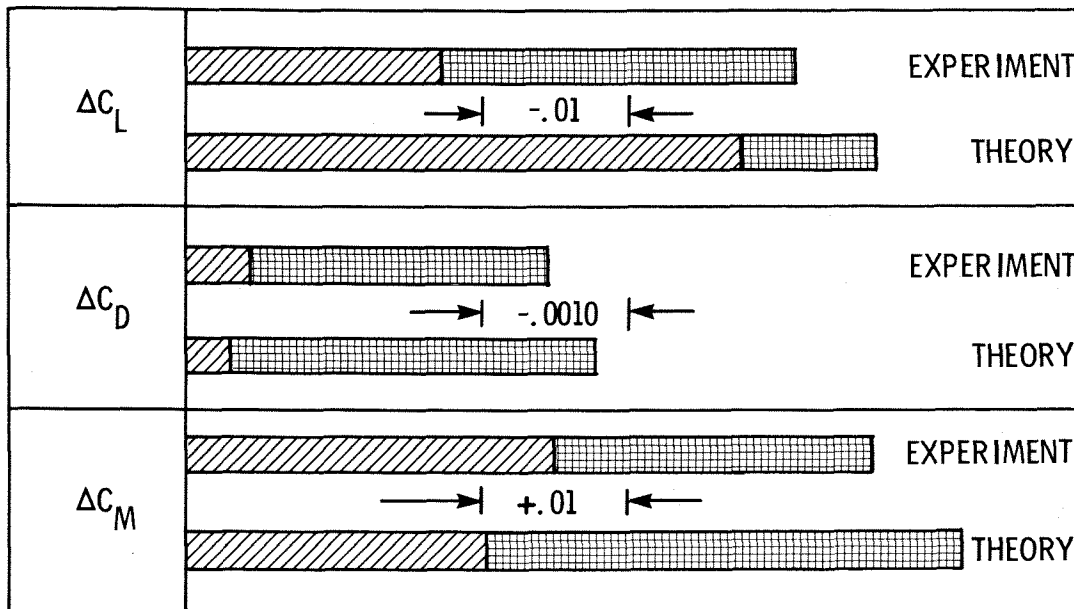
TABLE I.- COMPUTATIONAL REQUIREMENTS

CONFIGURATION	SECONDS/ITERATION	
	CYBER 175	CYBER 203
Isolated body	2.7	1.1
Wing alone	3.6	1.4
Wing/Body (crude)	3.5	1.4
Wing/Body/Pod (fine)	8.1	3.2
Wing/Body/Pylon/Pod	6.4	2.5

TABLE II. COMPARISON OF INCREMENTAL FORCES AND MOMENTS BETWEEN THE THREE WING PLANFORMS

$M = .82$   
 $\alpha = 2.2^\circ$

 TE EXT - BASELINE  
 LE EXT - TE EXT



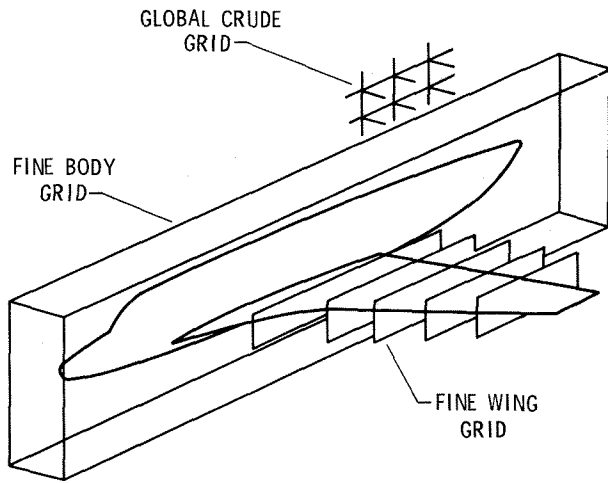


Figure 1. Crude grid system with embedded fine grid system.

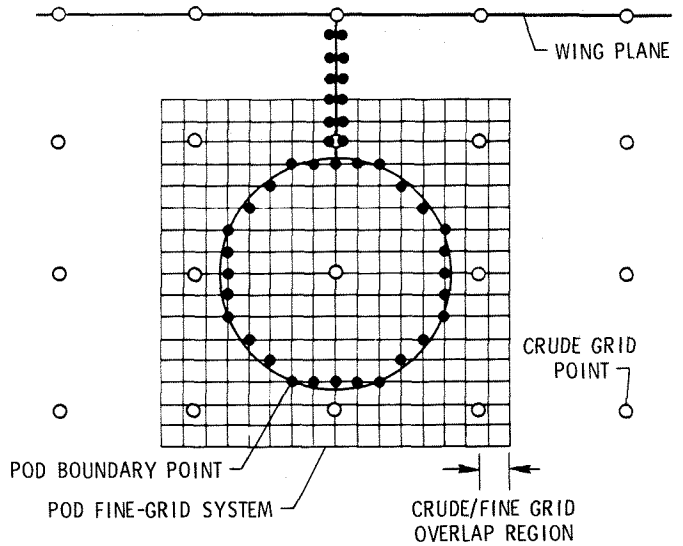
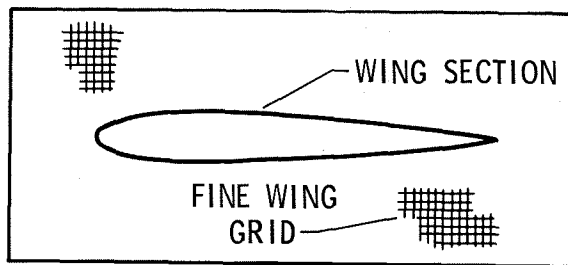
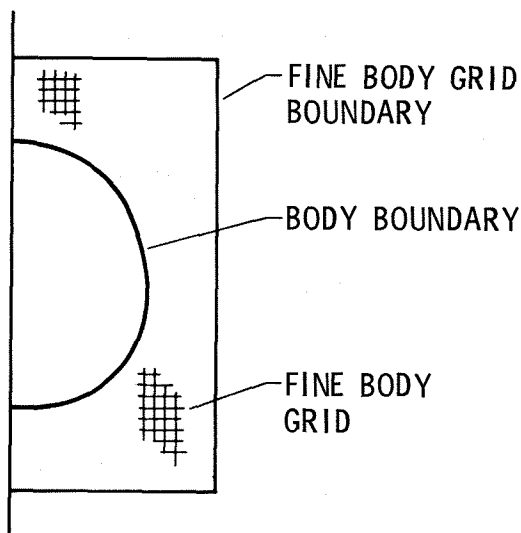


Figure 3. Crude/fine grid arrangement for pods and nacelles.



(a) Fine wing grid



(b) Fine body grid

Figure 2. Details of wing and body fine embedded grids.

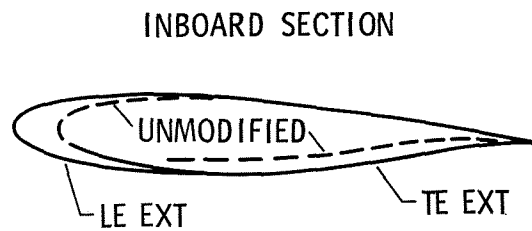
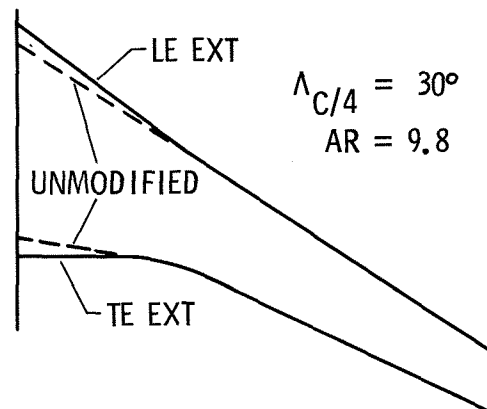


Figure 4. Root section and planform modifications to the selected wing.

$M = .82$   
 $\alpha = 2.2^\circ$

— BASELINE  
 - - - TRAILING EDGE EXTENSION

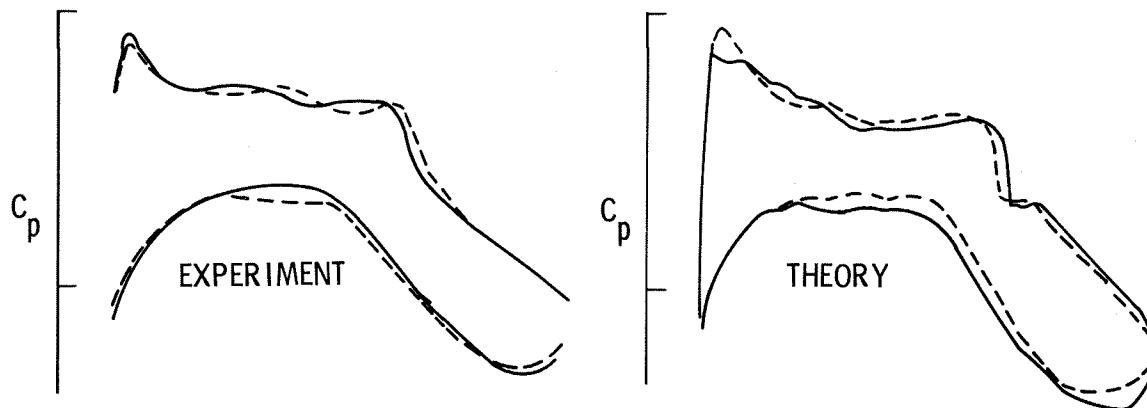


Figure 5. Comparison of pressure distributions between the baseline wing and trailing-edge modification.  $\eta = 0.25$

$M = .82$   
 $\alpha = 2.2^\circ$

— BASELINE  
 - - - TRAILING EDGE EXTENSION

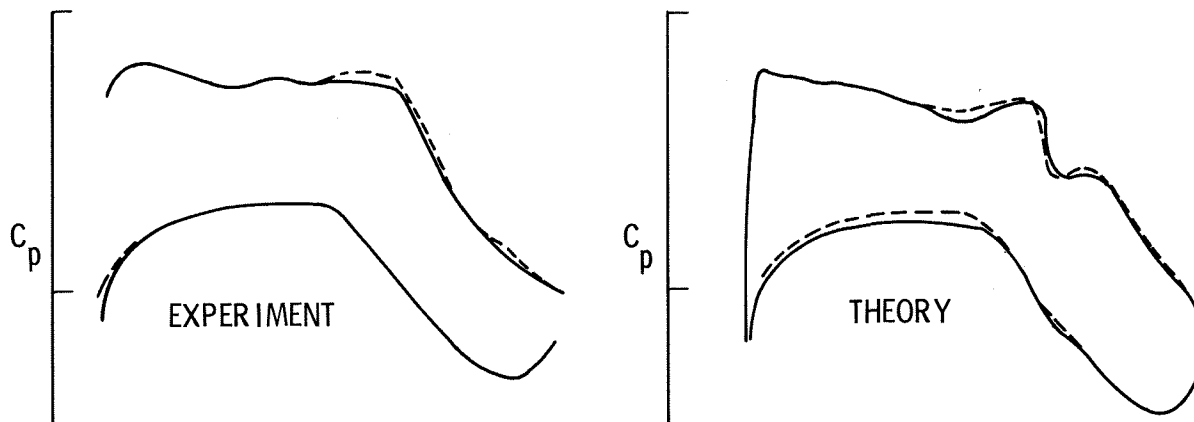


Figure 6. Comparison of pressure distributions between the baseline wing and trailing-edge modification.  $\eta = 0.41$

$M = .82$   
 $\alpha = 2.2^\circ$

— TRAILING EDGE EXTENSION  
 - - - LEADING EDGE EXTENSION

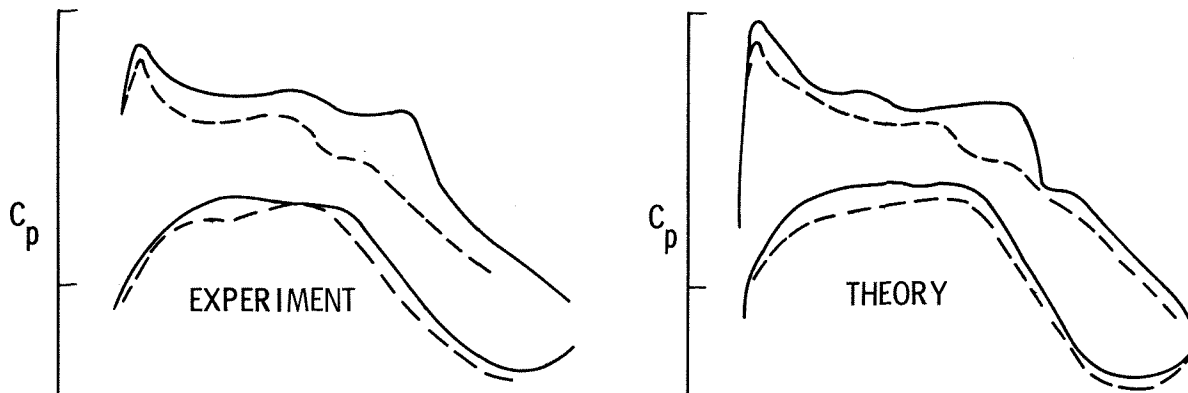


Figure 7. Comparison of pressure distributions between the trailing-edge and leading-edge modifications.  $\eta = 0.25$

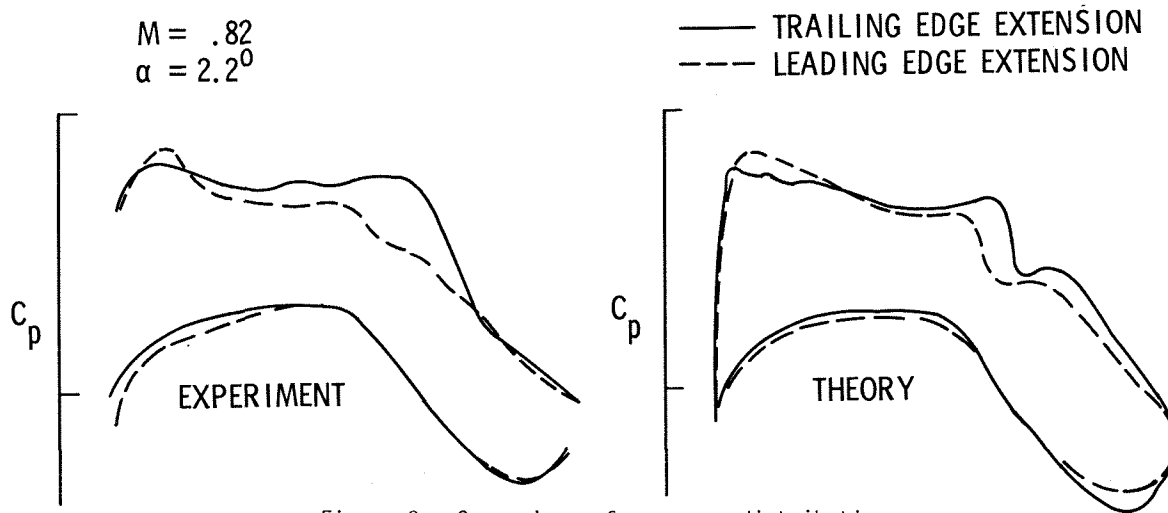


Figure 8. Comparison of pressure distributions between the trailing-edge and leading-edge modifications.  $\eta = 0.41$

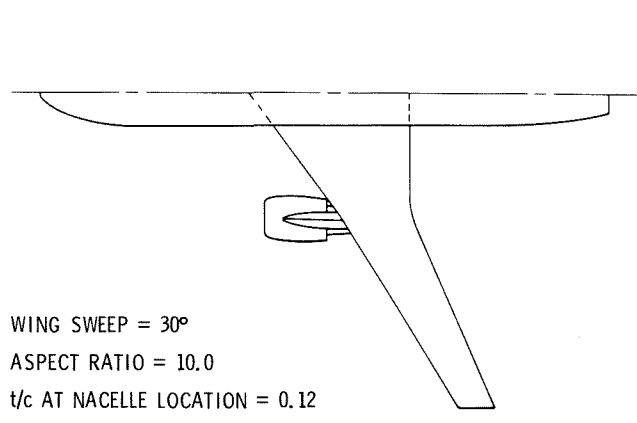


Figure 9. EET checkcase configuration.

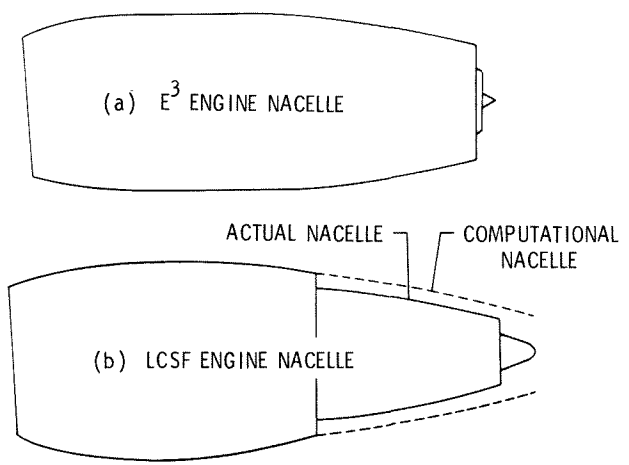


Figure 10. Engine nacelles used in validation.

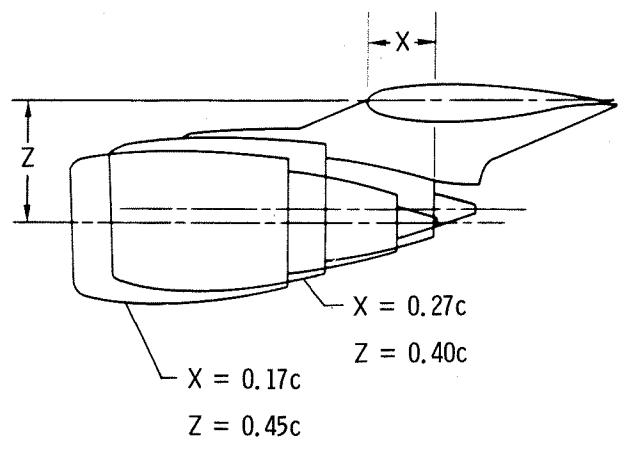


Figure 11. Variation of nacelle position.

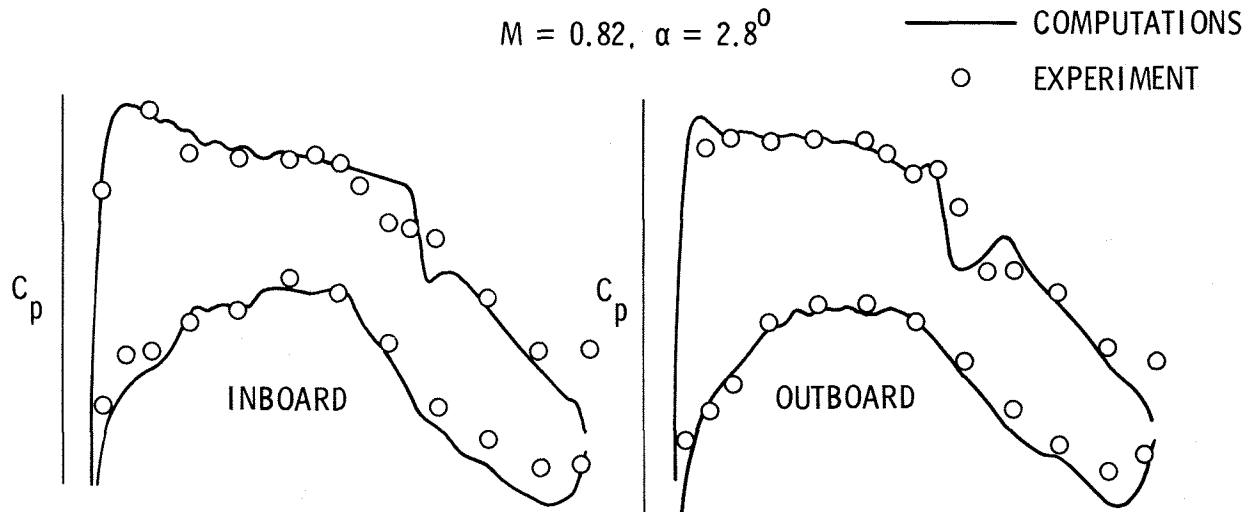


Figure 12. Comparison of computational results on checkcase configuration with experimental data.

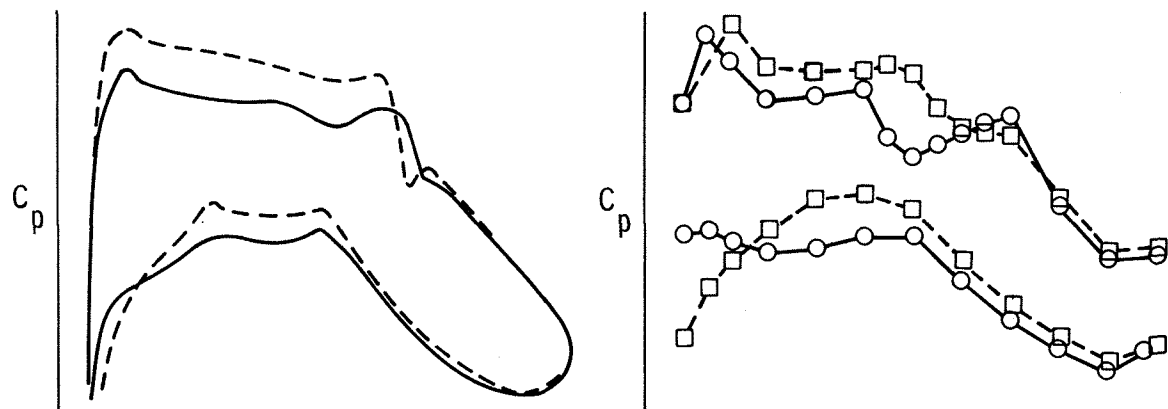
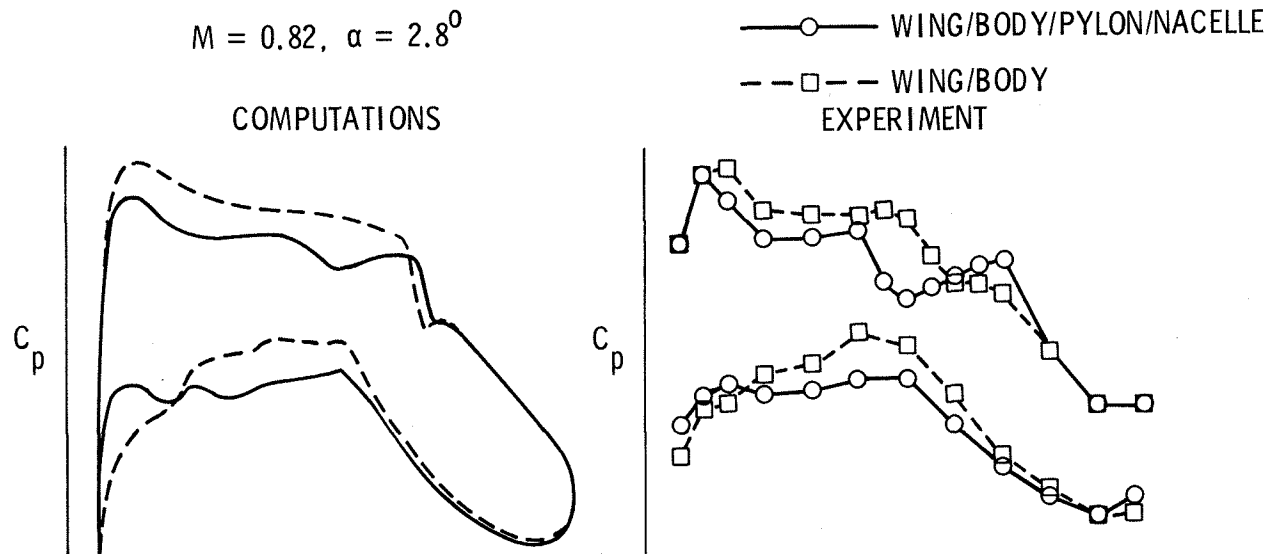


Figure 13. Comparison of computational results on wing/body/pylon/nacelle configuration with experimental data - E<sup>3</sup> engine nacelle.

$$\eta = 0.40, M = 0.82, \alpha = 2.8^\circ$$

EXIT	CL	COMP	EXP
0.17	0.40	————	○
0.27	0.40	-----	□

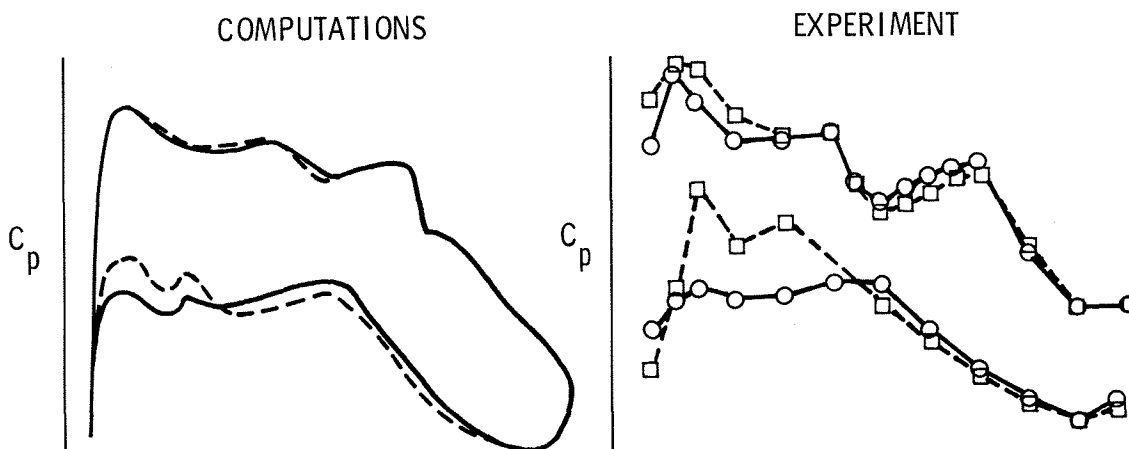


Figure 14. Comparison of computations and experiment for aft translation of E<sup>3</sup> engine nacelle.

$$\eta = 0.40, M = 0.82, \alpha = 2.8^\circ$$

EXIT	CL	COMP	EXP
0.40	0.40	————	□
0.25	0.45	-----	○

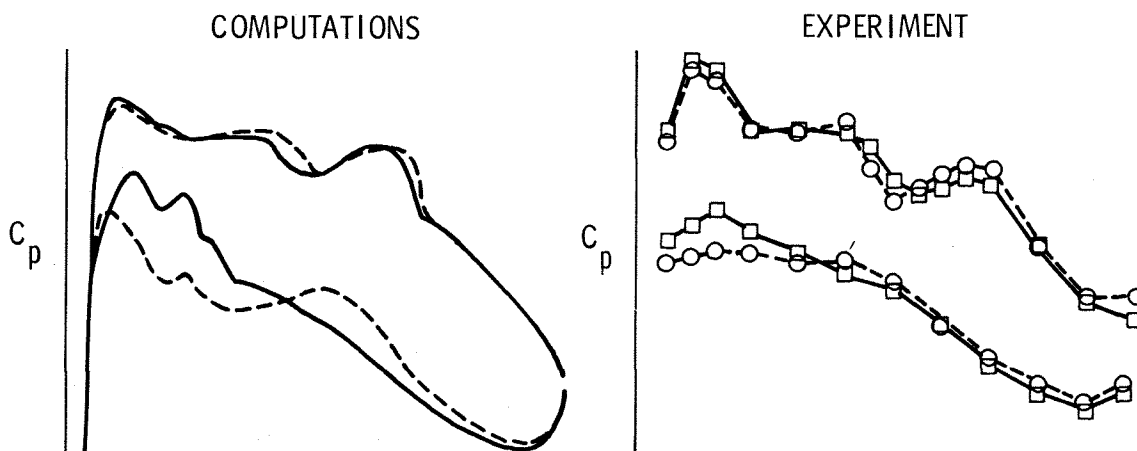


Figure 15. Comparison of computations and experiment for translation of LCSF engine nacelle.